Swirling motion in a system of vibrated elongated particles

Igor S. Aranson,[1] Dmitri Volfson,[2] and Lev S. Tsimring[2]
[1]*Argonne National Laboratory, 9700 South Cass Avenue, Argonne, Illinois 60439, USA*
[2]*Institute for Nonlinear Science, University of California, San Diego, La Jolla, California 92093, USA*
(Received 1 November 2006; published 1 May 2007)

Large-scale collective motion emerging in a monolayer of vertically vibrated elongated particles is studied. The motion is characterized by recurring swirls, with the characteristic scale exceeding several times the size of an individual particle. Our experiments identified a small horizontal component of the oscillatory acceleration of the vibrating plate in combination with orientation-dependent bottom friction (with respect to horizontal acceleration) as a source for the swirl formation. We developed a continuum model operating with the velocity field and local alignment tensor, which is in qualitative agreement with the experiment.

DOI: 10.1103/PhysRevE.75.051301 PACS number(s): 45.70.Qj, 05.65.+b

I. INTRODUCTION

Large-scale collective behavior emerging in systems of so-called self-propelled particles such as animals, birds, fish, swimming microorganisms, molecular motors, and even cars continues to attract enormous attention [1–14]. While vastly different in nature, these self-propelled particles often show similar behavior, e.g., long-range orientational order in two dimensions and collective directed motion.

Recent quasi-two-dimensional experiments with swimming bacteria [9,11] and vibrated anisotropic granular materials [15] exhibited surprising similarities between these two very different systems: at high enough concentration of elements both systems show onset of large-scale motion occurring in the form of recurring transient swirls and jets with the characteristic scale considerably exceeding the size of the individual element [15,16]. This similarity is puzzling because the bacteria used in Refs. [9,11] were polar particles (they were propelled by the rotation of the helical flagella without noticeable tumbling) and the anisotropic grains (e.g., rice, pins, etc.) were apparently apolar [15,16].

Recurring swirls of swimming bacteria were studied in recent experiments [9,11]. In Ref. [11], the rodlike bacteria *Bacillus subtilis* (4–5 μm long and about 1 μm wide) were confined to a 2–3 μm thick free-hanging liquid film. These microorganisms self-organized in spectacular dynamic structures with a characteristic scale exceeding the size of one bacterium by an order of magnitude. The onset to collective swimming occurs only when the number density of bacteria exceeds the critical value; otherwise the bacteria swim individually, and the correlation length of the corresponding velocity field is of the order of one microorganism length, i.e., 5 μm.

Visually similar swirls were also observed in recent experiments with vibrated anisotropic granular materials [15]. The authors of Ref. [15] suggested that the large-scale swirling behavior was related to "stray chirality" and defect motion. These swirls appeared to be very different from the vortices observed in earlier experiments [13] with larger-aspect-ratio particles and for larger plate acceleration. In those earlier experiments, dense islands of almost vertical rods were spontaneously formed within a thick layer of almost horizontal but orientationally disordered rods. As shown in Refs. [13,17], the quasivertical rods typically moved in the direction of the tilt, i.e., they effectively became polar self-propelled objects. Long-term evolution of these islands leads to coarsening and creation of a single vortex rotating in the direction given by the initial conditions. In contrast, in the experiments of [15] the filling fraction was much smaller, so only a monolayer of horizontal rods could be formed. At such a small filling fraction, rods do not reorient vertically; furthermore, they were confined to almost horizontal orientation by a lid. Thus, the particles in the experiment of [15] were vibrated symmetrically and were essentially apolar.

In this paper we focus on the physical mechanism leading to the onset of the swirling state in monolayers of vibrated quasihorizontal granular rods. Our experiments unambiguously identified the horizontal twisting component of bottom plate oscillations as a primary source of the overall collective grain motion. This periodic horizontal acceleration leads to the vibrational transport of particles; however, anisotropy of the particles provides the dependence of the friction force on the particle orientation with respect to driving acceleration and leads to the instability and swirl formation [18]. On the basis of experimental observations we develop a mathematical model reproducing on a qualitative level salient features of the experiment. Surprisingly, in a certain limit our model for vibrated apolar grains driven by a symmetry-breaking directional force is similar to that of polar bacteria in two dimensions [19], despite the obvious differences between these two systems. This coincidence suggests that the horizontal component of plate vibrations provides effective polarity to particles, and thus the similarity between swirling patterns in swimming bacteria and vibrated rods is not superficial but in fact is rooted in the underlying physics.

II. EXPERIMENTAL SETUP

Our experimental setup is similar to that described in Refs. [20,21]. We placed a monolayer of almost horizontal elongated grains in a 14 cm circular container vibrated vertically by an electromagnetic shaker. The bottom plate of the container was made of an optically flat silicon wafer. The experiments were performed in the range of 2.5 to 6 accelerations of gravity g and frequencies from 120 to 150 Hz at

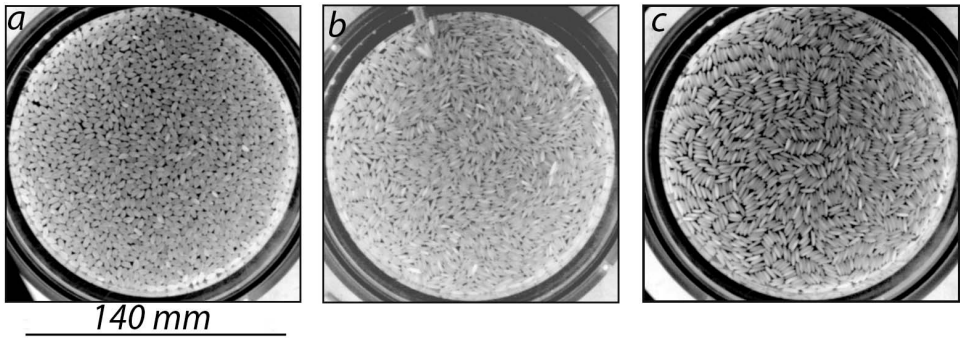

FIG. 1. Snapshots of patterns observed in experiments with vertically shaken long grains: (a) sushi rice, vertical acceleration $\Gamma=3g$ (g is the acceleration of gravity), frequency $f=133$ Hz; (b) jasmine rice, $\Gamma=2g$, $f=142$ Hz; (c) Basmati rice, $\Gamma=3.2g$, $f=133$ Hz. Vibrated Basmati rice demonstrated a significant amount of local smectic order, while jasmine and sushi rice showed local weakly nematic order (on the scale of 5–6 grains) and significant swirling. See also movie no. 1 in [22]. In all images filling fraction is about 85%.

atmospheric pressure. As granular media we used relatively large particles: sushi rice (mean length of the order 4 mm, aspect ratio 2–2.5), intermediate jasmine rice (mean length about 7 mm, aspect ratio 3.5–4), longer and thinner Basmati rice (mean length about 8 mm, aspect ratio about 6–8), nearly spherical mustard seeds (diameter about 2 mm), monodisperse stainless steel dowel pins (length 4 mm, aspect ratio 4), and monodisperse steel tumbling media particles (length about 6 mm, aspect ratio 6, tapered ends). We did not use an upper confining lid since the vertical plate oscillations (about 0.1 mm) were typically smaller than the particle diameter, and gravity confined the particles in a monolayer. Figure 1 shows examples of patterns observed in these experiments with different types of rice.

To monitor all components of the plate acceleration we used triaxial MMA7261Q accelerometers with sensitivity up to 800 mV/g. Two accelerometers were attached at the same radial distance from the center of the bottom plate and separated by a 90° angle (see Fig. 2). The amplitudes and phase differences between various acceleration components were monitored simultaneously by two EG&G lock-in amplifiers. The visual information was obtained from a digital RedLake camera suspended above the cavity. The camera resolution is up to 1024×1024 pixels with the capability of storing up to 7000 full-resolution images.

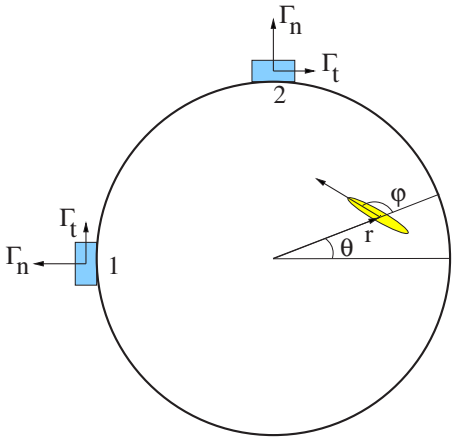

FIG. 2. (Color online) Sketch illustrating geometry of the experiment.

III. BULK ROTATION AND SWIRLING

For a wide range of particles we observed overall rotation of the pattern with the angular frequency ω dependent on the frequency f and the amplitude Γ of the plate acceleration. Almost rigid-body rotation was observed for both spherical mustard seeds and dowel pins (aspect ratio 4). For jasmine and sushi rice particles, rigid-body rotation was accompanied by a significant swirling motion. The swirls typically showed nonstationary behavior and often drifted around the container. Well-pronounced large-scale swirling motion occurred only at almost close-packed filling fraction (of the order of 85%). Practically no swirling was observed at lower filling fractions.

To quantify the collective motion of grains, we extracted the velocity field from the sequences of snapshots using standard particle image velocimetry [23]. Figure 3 shows the two-dimensional field of velocity (see also movies no. 2 and no. 3 in Ref. [22]). One sees up to four recurrent vortices or swirls with the characteristic size of about a quarter of the container diameter persisting in the course of an experiment.

Figure 4 presents the average angular velocity of the solid-body rotation component of the velocity field as a function of plate acceleration and frequency. As follows from the figure, the rotation angular velocity ω depends strongly on the vibration frequency f and on the vertical acceleration Γ_z. The angular velocity has a pronounced resonance peak at $f\approx130$ Hz and then changes sign at $f=134$ Hz. At this frequency we observed surprising switching behavior: the an-

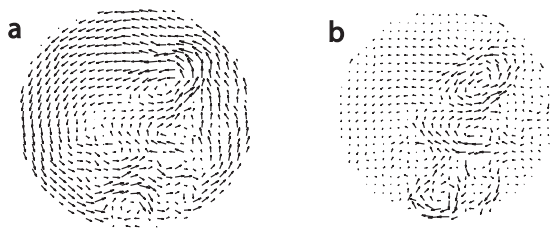

FIG. 3. (a) Velocity field obtained by the particle-image velocimetry technique [23] of the experimental movie for the jasmine rice at acceleration $2g$ and frequency $f=142$ Hz [parameters of Fig. 1(b)]; (b) velocity field with overall solid-body rotation subtracted. See also movies no. 2 and no. 3 in [22].

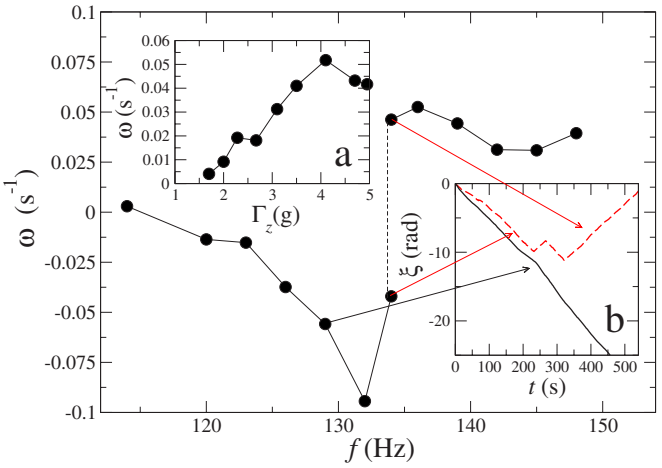

FIG. 4. (Color online) Average angular velocity ω as a function of frequency f for vertical acceleration $\Gamma_z=3.1g$ for 23.8 g of jasmine rice grains. Inset (a): ω vs acceleration Γ_z at $f=142$ Hz. Inset (b): total rotation phase $\xi, \omega=\dot{\xi}$ vs time for $f=129$ (solid line) and 134 (dashed line). See movie no. 4 in [22].

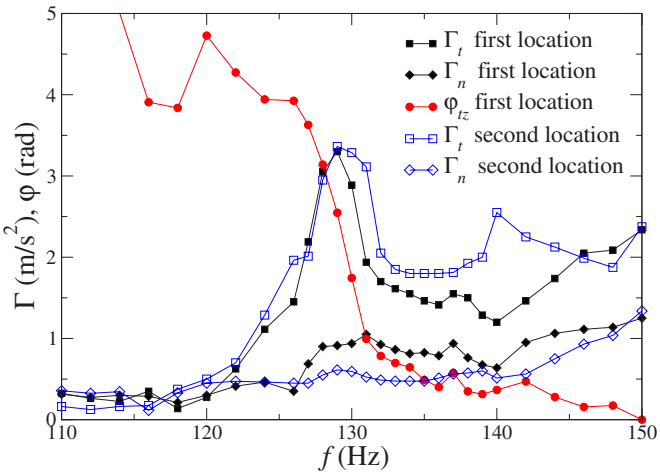

FIG. 5. (Color online) Tangential Γ_t (squares) and normal Γ_n (diamonds) components of acceleration at two different locations vs frequency f at fixed vertical acceleration $\Gamma_z=3.5g$. Line with circles depicts the phase difference φ_{tz} between vertical Γ_z and tangential Γ_t components of acceleration at the first location.

gular velocity randomly switches between positive and negative values [see Fig. 4, inset (b) and see also movie no. 4 in Ref. [22]]. Dependence on the vertical acceleration is nonmonotonic: the rotational velocity ω initially increases with the acceleration Γ_z almost linearly, reaches a maximum value at $\Gamma_z \approx 4g$, and finally decreases.

The overall rotation appears to be a bulk effect weakly dependent on the boundary conditions at the lateral wall. To verify that, we glued strips of rough sandpaper or a plastic cable tie with asymmetric teeth to the sidewall, but it did not affect the rotation in the bulk. Moreover, to exclude boundary effects we performed studies of a highly dilute gas of particles (ten particles only). Even so, each individual particle showed a tendency to move along circular trajectories (see discussion later).

In order to pinpoint the underlying mechanism of the rotation, we simultaneously measured, using lock-in amplifiers, the amplitudes of three components of plate acceleration and their relative phases at two locations at the edge of the plate orthogonal with respect to its center (see Fig. 2). The results are presented in Fig. 5. The measurements show that in a wide range of frequencies there was a significant component of horizontal acceleration tangential to the container's wall Γ_t. The amplitude of this tangential (or azimuthal) acceleration significantly exceeds the amplitude of the normal acceleration Γ_n. Moreover, the Γ_t values almost coincide at the two locations. These measurements demonstrate that in our experiments, in a wide range of frequencies, the bottom plate performed significant horizontal twisting vibrations around the center, synchronized to much stronger vertical vibrations. However, since the values of the tangential acceleration at two different positions do not coincide exactly, a small linear acceleration in a certain horizontal direction is present as well.

Furthermore, the angular velocity of rotation, ω, appears to be correlated with the amplitude of azimuthal acceleration, Γ_t (compare Figs. 4 and 5). These plots suggest that there is a resonance for the twisting mode vibrations near the frequency 130 Hz. Incidentally, near this frequency, the overall rotation of grains changes direction. This change of the rotation direction appears to be related to the rapid change of the relative phase φ between Γ_z and Γ_t near the resonant frequency. The exact value of the resonant frequency appears to depend on the amount of material loaded onto the vibrated plate. While it did not change significantly for rice (the total weight of a monolayer of rice in our experiment was 24 grams), for heavy steel pins (the total weight of a monolayer of pins was about 200 grams) we noticed a significant shift of the resonance.

Thus, our measurements are consistent with the conjecture that the overall rotation of grains around the cavity center is caused mainly by the phase shift between the horizontal twisting and the vertical vibrations of the bottom plate [24]; this mechanism is widely used in the design of vibroconveyors [25,26]. Note that, at large amplitude of plate vibration, the amplitude and the direction of the rod transport are determined by a complex interplay of both the amplitude of vibrations and the phase shift between horizontal and vertical vibrations [26] (see also [13]); however, at relatively small amplitude of plate vibrations, the phases of the horizontal and vertical components appear to be the dominant factor.

Unlike the case of simple spherical or nearly spherical grains, for elongated particles, in addition to the overall rotation of the granular monolayer, we observed a significant swirling motion with a characteristic spatial scale that is less than the system size but still much larger than individual grain size (see the movies in [22]). This swirling motion was not observed in similar experiments with mustard seeds. In contrast to Ref. [15], in our experiments the swirling motion was observed for several different types of rice and in a wide range of parameters. It is probably explained by the fact that in our system the amplitude of the horizontal acceleration was larger than in that of [15]. A typical velocity pattern in the swirling state after the removal of the solid-body rotation is shown in Fig. 3(b).

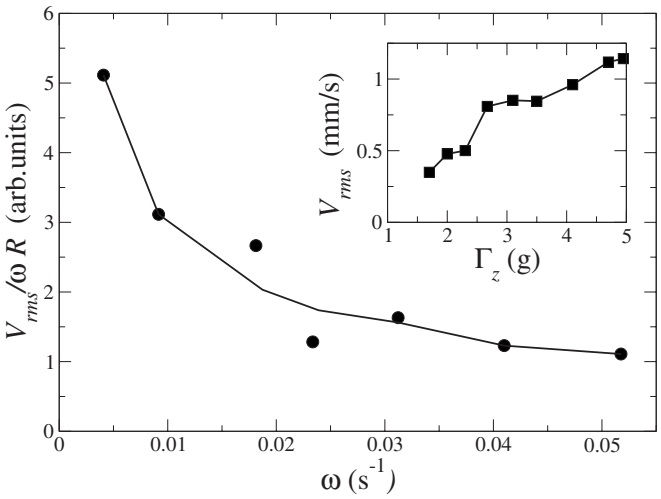

FIG. 6. rms velocity of swirling motion, V_{rms}, normalized by the maximum linear velocity of the solid-body grain rotation, ωR (R is the radius of the container) for vibration frequency $f=142$ Hz vs the rotation frequency ω for 23.8 grams of jasmine rice. Experimental points are shown as filled circles; the solid line is a guide for the eye. Inset: V_{rms} vs vertical acceleration Γ_z.

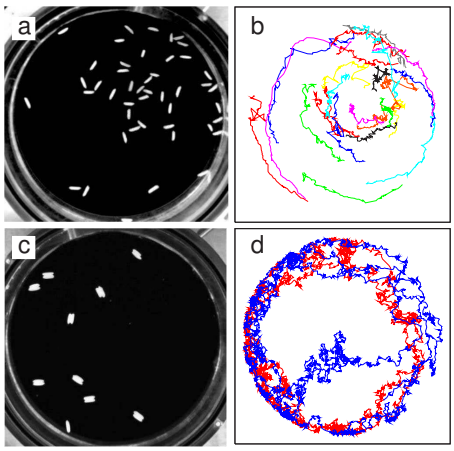

FIG. 7. (Color online) (a) Typical snapshot of several monomer grains drifting on a vibrated plate at $f=133$ Hz and $\Gamma_z=3.5g$. See also movie no. 5 in [22] for particle trajectories. (b) Trajectories of two grains extracted from the sequences of snapshots using custom Interactive Data Language–based [27] image segmentation software. (c), (d) The same for catamaran particles in a similar vibration regime, $f=129$ Hz, $\Gamma_z=3.5g$. See also movie no. 6 in [22] for particle trajectories.

In order to characterize the swirling motion we calculated the corresponding root mean square (rms) averaged velocity V_{rms} after the removal of the solid-body rotation component of velocity:

$$V_{rms} = \sqrt{\langle |\mathbf{V} - \mathbf{V}_{rot}|^2 \rangle} \tag{1}$$

where $V_{rot}=\omega r$ is the linear velocity of rotation at the radius r from the rotation center. The average is taken over all surface of the container. Accordingly, the V_{rms} value for pure solid-body rotation is zero. The corresponding dependence of V_{rms} on the vertical acceleration Γ_z is shown in Fig. 6, inset. In this figure, one can see a tendency toward increased swirling velocity V_{rms} with increase of acceleration. However, the swirling velocity normalized by the rotational velocity ωR decreases with increase of the angular velocity ω, which represents the magnitude of the driving force (see Fig. 6). This observation suggests that the relative strength of swirls is in fact larger at small accelerations where the rotation velocity is smaller.

IV. PROPERTIES OF A DILUTE GAS OF VIBRATED ELONGATED PARTICLES

Solid-body rotation and swirling motion are of course collective phenomena which emerge through the interaction of many grains. However, the source of this motion must lie in the dependence of the momentum transfer from the vibrated plate to the elongated grains on the orientation of the grains. In order to separate this effect from collisional interactions of grains, we conducted experiments with a highly dilute system (about 10–20 particles only).

We recorded the positions and orientations of individual grains following several long particle trajectories [see Figs. 7(a) and 7(b)]. Due to the cylindrical geometry of our experiment, the position of a particle is characterized in polar coordinates by the radius r and polar angle θ, and the orientation of the particle is characterized by the angle ϕ with respect to the radial direction (see Fig. 2). Processing about 10^6 data points, we accumulated velocity distributions for different grain orientations ϕ with respect to the vector from the center of the cavity to the grain position. These distributions show clear signs of anisotropy (see Fig. 8). The most obvious feature of these distributions is that their centers are shifted toward positive values of V_θ, which indicates overall counterclockwise rotation of grains around the cavity center. This is also evident from the particle trajectories (Fig. 7). Furthermore, the widths of the distributions in radial and azimuthal direction, and correspondingly the standard deviations σ_{V_r} and σ_{V_θ}, are also different. For $\phi=0$ (the particle is oriented along the radius), standard deviations $\sigma_{V_\theta} > \sigma_{V_r}$, while for $\phi=\pi/2$ the relation is opposite. We also found that the distributions for $\phi=0$ (radial orientation of grains) were slightly tilted, which indicates the presence of asymmetry of vibrational driving; however, the specific origin of this anisotropy is not clear. Figure 9 shows the dependence of the standard deviations σ_{V_r} and σ_{V_θ} on the orientation angle ϕ. This dependence is consistent with a simple model that the grains are driven by a force with nonzero mean acting predominantly in the azimuthal direction, plus a strong isotropic fluctuating component, and they are damped by an orientation-dependent frictional force ($\mathbf{V}$ is the particle velocity with respect to the container bottom), which can be cast in the following form:

$$\hat{\mathbf{B}}\mathbf{V} = \mathbf{F}_0 + \xi(t) \tag{2}$$

where $\hat{\mathbf{B}}$ is a 2×2 "friction" matrix, $\xi(t)$ is the white noise modeling the effect of vibration, and $\mathbf{F}_0$ is the driving force.

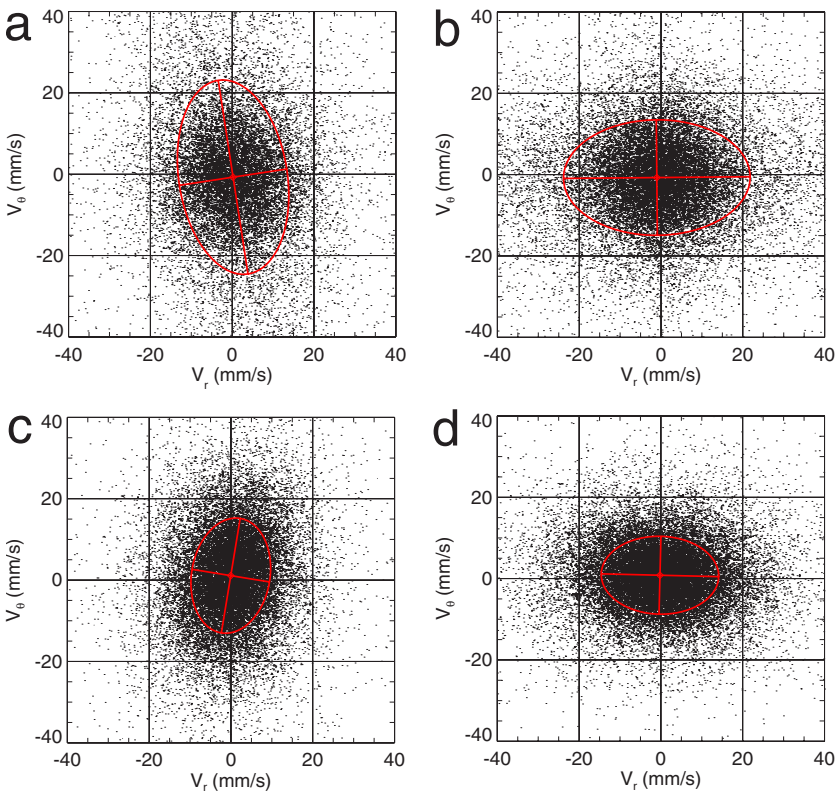

FIG. 8. (Color online) Velocity distribution functions of isolated particles (a), (b) and catamarans (c), (d) for $f=129$ Hz and $\Gamma_z=3.5g$. V_θ and V_r are azimuthal and radial components of particle velocity. (a), (c) correspond to grains oriented in the azimuthal and (b), (d) in the radial directions. Inertial ellipses shown in red (gray) have main radii equal to the standard deviations of the corresponding distributions in the directions of the main axes.

On symmetry grounds the friction matrix $\hat{B}$ in the first order can be written as

$$B_{ij} = \beta_0 \delta_{ij} + \beta_1 (2 n_i n_j - \delta_{ij}) \tag{3}$$

where the coefficients β_0 and β_1 characterize isotropic and anisotropic contributions, $\{i,j\} \in \{\parallel, \perp\}$, and $n_{\parallel,\perp}$ are projections of the grain director on the direction of particle translation and the orthogonal direction, respectively. In our circular geometry when the driving force is directed azimuthally, particles move predominantly in the azimuthal direction, and $n_\parallel = \cos\phi, n_\perp = \sin\phi$, so the friction tensor can be written as

$$\hat{B} = \beta_0 \mathbf{I} + \beta_1 \begin{pmatrix} \cos(2\phi) & \sin(2\phi) \\ \sin(2\phi) & -\cos(2\phi) \end{pmatrix} \tag{4}$$

where $\mathbf{I}$ is the identity matrix. For positive β_1, this expression implies that friction is maximal when the particle is translated along itself and minimal when it is translated in the perpendicular direction. This expression will be used later for the description of dense phase flows. In the dense phase, the stochastic component of the driving force should be strongly suppressed due to confinement by neighboring grains, but the anisotropy of friction still would be a significant factor in the selection of a flowing regime. Using Eqs. (2) and (4), for small anisotropy ($\beta_1 \ll \beta_0$) one can derive the standard deviations of velocity ($\sigma_{V_\theta}, \sigma_{V_r}$) as functions of the orientation ϕ:

$$\sigma_{V_\theta} = \sigma_0 \left(1 - \frac{\beta_1}{\beta_0} \cos(2\phi) \right),$$

$$\sigma_{V_r} = \sigma_0 \left(1 + \frac{\beta_1}{\beta_0} \cos(2\phi) \right) \tag{5}$$

which fit well with the experimental data (Fig. 9).

The anisotropic friction should also lead to the dependence of the mean azimuthal velocity V_θ on the orientational angle ϕ. Assuming that the driving force F_0 is oriented along the azimuthal direction only, by balancing the driving force to the friction force Eq. (2) we obtain

$$\langle V_\theta \rangle = \frac{F_0}{\beta_0} \left(1 - \frac{\beta_1}{\beta_0} \cos(2\phi) \right) + O(\beta_1^2/\beta_0^2). \tag{6}$$

However, we were not able to reliably confirm this dependency in experiments with individual particles [see Fig. 9(a)] probably due to large velocity fluctuations (the standard deviation of the velocity is an order of magnitude greater than the mean). These large velocity fluctuations are likely related to rolling and bouncing of individual grains, shadowing the effect of the anisotropic sliding.

In order to reduce this effect and suppress at least the rolling motion of grains, we glued pairs of particles together to form "catamaran" objects [Figs. 7(c) and 7(d)]. The results of data processing for catamaran particles at the same conditions ($f=129$ Hz, $\Gamma_z=3.5g$) are shown in Figs. 8(c), 8(d), and 9(b). These data show evidence of mean velocity anisotropy consistent with the anisotropic friction hypothesis, Eq. (6) [see Fig. 9(b)]. However, it can be fitted with Eq. (6) only up to a certain phase shift $\Delta\phi \approx -0.34$. Most likely this phase shift originates from the fact that in our experiment plate vibrations have both azimuthal and linear modes of horizontal displacement (see Fig. 5). Consequently, the driving force

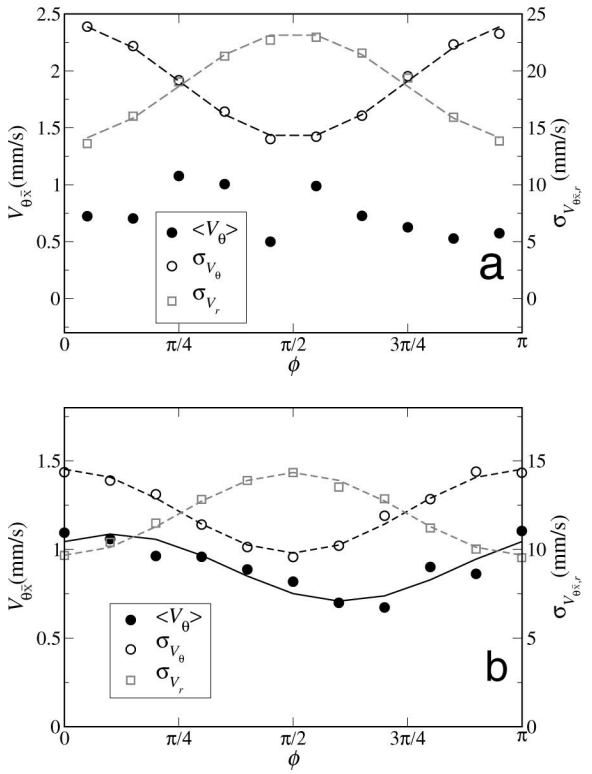

FIG. 9. Statistical characteristics of velocity distributions for individual particles (a) and catamarans (b) for a run at $f=129$ Hz and $\Gamma_z=3.5g$: Average azimuthal velocity V_θ (solid black circles) and standard deviations of V_θ and radial velocity V_r, σ_{V_θ} and σ_{V_r}, as functions of the angle ϕ between the particles and the radius vector from the center of the cavity to the center of the particle. Dashed lines show fits of the data by the sinusoidal functions expected for driven particles with anisotropic friction force in the linear approximation (5) and (6). For individual particles the best fit yields for the standard deviations $\sigma_{V_\theta}=19.1+4.95\cos(2\phi)$ and $\sigma_{V_r}=19.1-4.95\cos(2\phi)$ (a). For catamaran particles (b) the fit to experimental data yields $\sigma_{V_\theta}=12.1+2.33\cos(2\phi)$, $\sigma_{V_r}=12.1-2.33\cos(2\phi)$ for the standard deviations and for the average azimuthal velocity $V_\theta=0.87+0.19\cos[2(\phi-0.34)]$, respectively.

was not purely tangential (the ratio of $|\Gamma_n/\Gamma_t|\approx 0.2$), which can skew the dependence of mean azimuthal velocity $\langle V_\theta\rangle$ vs the orientational angle ϕ.

Figure 10 shows the azimuthal and radial velocity probability distribution functions calculated using data for all orientations of grains. As one sees, the velocity distributions are symmetric ($\sigma_{V_\theta}\approx\sigma_{V_r}$) but strongly non-Gaussian, with noticeably overpopulated tails, arising likely from the inelasticity of particle collisions and the anisotropy of particle interactions [28,29].

V. MATHEMATICAL MODEL

In the hydrodynamic description the nematic ordering of rice particles can be characterized by the symmetric traceless alignment tensor $\mathbf{Q}$ related to the nematic director $\mathbf{n}=(\cos\tilde{\phi},\sin\tilde{\phi})$ as follows

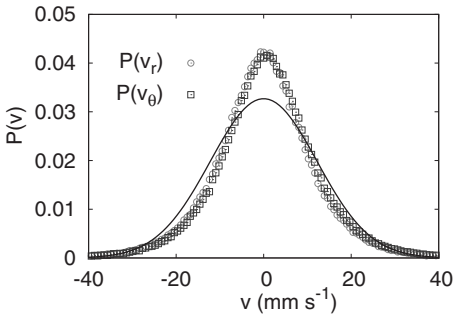

FIG. 10. Probability distribution functions for azimuthal V_θ and radial V_r velocity components of catamaran particles normalized by corresponding dispersions σ_{V_θ} and σ_{V_r} at $f=129$ Hz and $A_z=3.5g$. Gaussian distribution with the same variance is shown for comparison by a solid line.

$$\mathbf{Q}=\frac{s}{2}\begin{pmatrix}\cos(2\tilde{\phi}) & \sin(2\tilde{\phi})\\ \sin(2\tilde{\phi}) & -\cos(2\tilde{\phi})\end{pmatrix} \tag{7}$$

where s is the magnitude of the order parameter ($s=0$ means total disorder, and $s=1$ corresponds to perfect nematic alignment), and $\tilde{\phi}$ is the mean grain orientation angle with respect to an arbitrary fixed direction within a mesoscopic area. Here we neglect the effects of the smectic ordering.

We are interested in time scales that are much larger than the period of the plate vibrations, so we shall ignore the vertical vibrations of individual grains and consider only two-dimensional in-plane transport. According to Refs. [3,30–34], the generic equation describing the evolution of the alignment tensor $\mathbf{Q}$ in two dimensions is of the form [35]

$$\frac{\partial\mathbf{Q}}{\partial t}+(\mathbf{v}\cdot\boldsymbol{\nabla})\mathbf{Q}=\epsilon\mathbf{Q}-\frac{1}{2}\mathrm{Tr}(\mathbf{Q}\cdot\mathbf{Q})\mathbf{Q}+D_1\nabla^2\mathbf{Q}+D_2\boldsymbol{\nabla}(\boldsymbol{\nabla}\cdot\mathbf{Q})+\boldsymbol{\Omega}\mathbf{Q}-\mathbf{Q}\boldsymbol{\Omega} \tag{8}$$

where $\mathbf{v}$ is the hydrodynamic velocity, $\boldsymbol{\Omega}=\frac{1}{2}[\boldsymbol{\nabla}\mathbf{v}-\boldsymbol{\nabla}\mathbf{v}^T]$ is the vorticity tensor (we assume that the flow of particles is incompressible), $D_{1,2}$ are the corresponding elastic constants (compare with liquid crystals [30]), and $\epsilon\sim\rho-\rho_c$ is the parameter controlling the nematic transition, which depends on the grain packing density ρ. Here ρ_c is the critical density of the nematic phase transition. For the hydrodynamic velocity $\mathbf{v}$ we have the following analog of the two-dimensional Navier-Stokes equations:

$$\partial_t\mathbf{v}+(\mathbf{v}\cdot\boldsymbol{\nabla})\mathbf{v}=\nu\boldsymbol{\nabla}^2\mathbf{v}-\boldsymbol{\nabla}p-\mathbf{F}_f(\mathbf{Q},\mathbf{v})+\mathbf{F},\quad \boldsymbol{\nabla}\cdot\mathbf{v}=0, \tag{9}$$

where ν is the shear viscosity of the granular flow (we neglect for simplicity the anisotropy of the viscosity), p is the hydrodynamic pressure, and $\mathbf{F}$ is the driving (or conveying) force due to mixed vertical and horizontal vibrations of the plate [36]. Here $\mathbf{F}_f(\mathbf{Q},\mathbf{v})$ is the anisotropic friction force between particles and the bottom. Using our experiential results for the friction force of catamaran particles, Eq. (2), we assume the following dependence of the friction force of the velocity $\mathbf{v}$ and alignment tensor $\mathbf{Q}$:

$$\mathbf{F}_f(\mathbf{Q},\mathbf{v}) = (\beta_0 + \beta_1 \mathbf{Q})\mathbf{v}. \tag{10}$$

In the following we focus on the limit of small anisotropy of friction coefficient, i.e., $\beta_1 \ll \beta_0$. In our experiment, the horizontal plate vibrations have predominantly the azimuthal component. To simplify the calculations we consider the limiting case of a very large container and introduce a local rectangular coordinate system instead of the cylindrical one. Then we choose the x direction along the horizontal component of plate acceleration, Γ_x, which we assume coincides with the direction of the driving force $\mathbf{F}$. Since the tensor $\mathbf{Q}$ has only two independent variables in two dimensions, it is useful to introduce a *quasivector* of local orientation

$$\boldsymbol{\tau} = (\tau_x, \tau_y) \equiv (Q_{xx}, Q_{xy}) = \frac{s}{2}(\cos 2\tilde{\phi}, \sin 2\tilde{\phi}), \tag{11}$$

where the angle $\tilde{\phi}$ is now between the director and the orientation of the driving force $\mathbf{F}$.

We further assume that the hydrodynamic velocity $\mathbf{v}$ is always close to the uniform translation velocity $\mathbf{v}_0 = \beta_0^{-1} F_0 \mathbf{x}_0$ (x_0 is a unit vector in the x direction which we choose to coincide with the direction of the mean driving force). Since $\beta_1 \ll \beta_0$, we can rewrite the hydrodynamic equation (9) in the form

$$\partial_t \mathbf{v} + (\mathbf{v}\cdot\boldsymbol{\nabla})\mathbf{v} = \nu\nabla^2\mathbf{v} - \boldsymbol{\nabla} p - \beta_0 \mathbf{v} + \alpha F_0 \boldsymbol{\tau} + O(\alpha^2) \tag{12}$$

where $\alpha = \beta_1/\beta_0$ is a small parameter. Equation (8) in the same approximation can be rewritten as

$$\frac{\partial \boldsymbol{\tau}}{\partial t} + (\mathbf{v}\cdot\boldsymbol{\nabla})\boldsymbol{\tau} = \epsilon\boldsymbol{\tau} - |\boldsymbol{\tau}|^2\boldsymbol{\tau} + D_1\nabla^2\boldsymbol{\tau} + D_2\boldsymbol{\nabla}(\boldsymbol{\nabla}\cdot\boldsymbol{\tau}) + \Omega \mathbf{z}_0 \times \boldsymbol{\tau}, \tag{13}$$

where $\Omega = (\partial_y v_x - \partial_x v_y)$ is the vorticity component directed along the vertical coordinate z, $\mathbf{z}_0$ is a unit vector in the z-direction.

In order to exclude pressure we take the curl of Eq. (12) and obtain the equation for the vorticity

$$\partial_t \Omega + (\mathbf{v}\cdot\boldsymbol{\nabla})\Omega = \nu\nabla^2\Omega - \beta_0\Omega + F_0\alpha(\partial_y\tau_x - \partial_x\tau_y). \tag{14}$$

Equations (13) and (14) form a closed system of equations.

Uniform transport of particles corresponds to the stationary solution $\tau_x = \tau_0$, $\tau_y = 0$, $v_y = 0$, $v_x = v_0 = (F_0 + F_0\alpha\tau_0)/\beta_0$, p = const, and $|\tau_0| = \sqrt{\epsilon}$. Here τ_0 is the magnitude of the order parameter characterizing local nematic order ($\tau_0 = 0$ corresponds to a disordered packing, and $|\tau_0| = \sqrt{\epsilon}$ corresponds to the aligned nematic state).

Now we examine the stability of this uniformly moving state to a periodic modulation with wave vector parallel to $\mathbf{F}_0$, since oblique perturbations have a smaller growth rate. Substituting the perturbed solution $(\tau_x, \tau_y, \Omega) = (\tau_0, 0, 0) + (\tilde{\tau}_x, \tilde{\tau}_y, \tilde{\Omega})\exp(\lambda t + ikx)$ into the linearized Eqs. (13) and (14) we obtain after simple algebra

$$\lambda\tilde{\tau}_x = -ikv_0\tilde{\tau}_x - 2\tau_0^2\tilde{\tau}_x - (D_1 + D_2)k^2\tilde{\tau}_x, \tag{15}$$

$$\lambda\tilde{\tau}_y = -ikv_0\tilde{\tau}_y - \tilde{\Omega}\tau_0 - D_1 k^2\tilde{\tau}_y, \tag{16}$$

$$\lambda\tilde{\Omega} = -ikv_0\tilde{\Omega} - \nu k^2\tilde{\Omega} - \beta_0\tilde{\Omega} - ikF_0\alpha\tilde{\tau}_y. \tag{17}$$

Thus, the equation for τ_x splits off and we need to deal with only equations for τ_y, Ω. They yield the matrix equation

$$\det\begin{pmatrix} -D_1k^2 - ikv_0 - \lambda, & -\tau_0 \\ -ikF_0\alpha, & -\beta_0 - \nu k^2 - ikv_0 - \lambda \end{pmatrix} = 0. \tag{18}$$

The roots of the characteristic polynomial are given by

$$\lambda_{1,2} = \frac{1}{2}\{-(D_1 + \nu)k^2 - \beta_0 - 2ikv_0 \pm \sqrt{[(D_1 - \nu)k^2 - \beta_0]^2 - 4ik\tau_0 F_0\alpha}\}. \tag{19}$$

The instability occurs in a finite range of wave numbers if the parameter $F_0\alpha$ is greater than some critical value. The eigenmode corresponding to the instability has the form of periodic undulations of the local orientation accompanied by the periodic shear. The onset of instability can be obtained in the long-wavelength limit $k \to 0$. Then Eq. (19) yields (using $|\tau_0|^2 = \epsilon$)

$$\mathrm{Re}\,\lambda = \left(\frac{2F_0^2\alpha^2\epsilon}{\beta_0^3} - D_1\right)k^2 + O(k^4). \tag{20}$$

This equation produces the threshold for the onset of long-wave instability,

$$2F_0^2\alpha^2\epsilon > \beta_0^3 D_1. \tag{21}$$

Thus the instability threshold is controlled by the value of the elastic constant D_1 and the friction parameter β_0, which depend on the shape and the aspect ratio of the particles.

The maximum growth rate occurs at a certain wave number k_m which is a function of the model parameters. The selected wave number k_m is easy to calculate in the limit of relatively large value of the speed v_0. Expanding Eq. (19) for $|F_0\alpha| \gg |(D_1 + \nu)k^2 - \beta|$ we obtain

$$\mathrm{Re}(\lambda) \approx \frac{1}{2}\left(-(D_1 + \nu)k^2 - \beta_0 + \sqrt{2|k|F_0\alpha\sqrt{\epsilon}}\right) + O\left(1/\sqrt{F_0\alpha}\right). \tag{22}$$

Then from Eq. (22)

$$k_M^{3/2} = \frac{\sqrt{2F_0\alpha\sqrt{\epsilon}}}{4(D_1 + \nu)}. \tag{23}$$

The associated length scale $L \sim 1/k_m$ determines the characteristic size of the swirls. In order to study the dynamics beyond the linear instability we performed numerical studies of Eqs. (13) and (14) in a periodic domain. A snapshot of a typical simulation in the parameter range corresponding to the linear instability is shown in Fig. 11. Figure 11(a) shows the director field $\mathbf{n}$ and Fig. 11(b) shows the velocity field $\mathbf{v}$. As seen from the figure, indeed the model exhibits an array of swirls, in agreement with the experiment.

In order to compare our results with the experiment more quantitatively, we calculated numerically the value of the rms velocity of swirling motion, V_{rms}, as a function of the

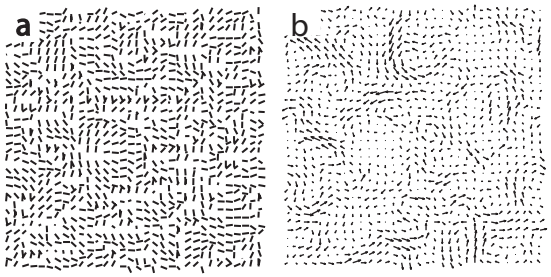

FIG. 11. Snapshots illustrating director field **n** (a) and velocity field **v** (b) from numerical simulations of the continuum model (8) and (14); see also movie in [22]. Parameters in Eqs. (13) and (14) are $\epsilon=1, \beta_0=0.2, \nu=3, D_1=0.8, D_2=0.4$, $F_0\alpha=1$, and integration is performed in a periodic domain of size 200×200 dimensionless units.

driving force F_0. We have found that, as in the experiment, the value of V_{rms} increases with F_0 (in the experiment of course we do not have direct measurements of the driving force, but we can infer it from measuring the overall rotation rate of grains around the cavity). Moreover, in a qualitative agreement with the experiment, the value of V_{rms} divided by the parameter $F_0\alpha$ decreases with the driving F_0, similar to the decrease of the normalized V_{rms} with solid-body rotation frequency ω (compare Figs. 6 and 12).

VI. CONCLUSIONS

In this work we studied the motion of a monolayer of elongated particles in a circular container with a vibrated bottom. Depending on the amplitude and frequency of vibrations and particle type, a variety of distinct pattern-forming phenomena were observed, from solid-body rotation in the system of spherical particles or cylinders to dynamic swirls and smectic structures. We demonstrated that the overall rotation of grains in the cavity was due to the presence, in addition to vertical vibration, of a small horizontal component of vibration predominantly in the form of an azimuthal twisting mode. The swirl formation, which was first observed in Ref. [15] and studied in more detail here, can be explained by an instability that is caused by the dependence of the bottom friction force on the particle orientation with respect to the direction of the driving force. The relation of the friction force anisotropy and the vibration parameters can be clarified in future studies by detailed three-dimensional calculations of the motion of an elongated particle bouncing on a vibrated plate as in Refs. [17,37]. The orientational ordering of grains leads to large-scale perturbations of the stress acting on particles, which in turn affect their orientational dynamics. Our theoretical model, based on a phenomenological equation for the alignment tensor coupled to the equation for the particle velocity, allowed us to describe this instability analytically. Numerical simulations of our continuum model yielded swirling patterns qualitatively similar to experimental ones.

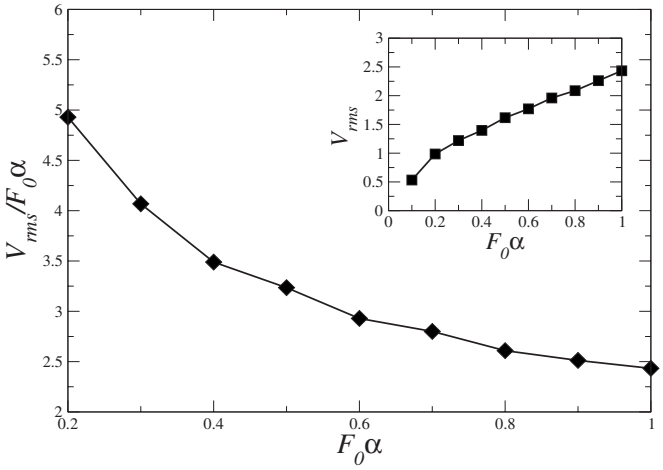

FIG. 12. rms velocity of swirling motion V_{rms} normalized by the parameter $F_0\alpha$ vs $F_0\alpha$. Other parameters as in Fig. 11. Inset: V_{rms} vs $F_0\alpha$. Parameters for Eqs. (13) and (14) are periodic integration domain size 200×200 units, $\epsilon=1, \beta_0=0.2, D_2=0.4, D_1=0.8, \nu=3$.

In this model we neglected the effects of smectic ordering visible in our experimental data [see Figs. 1(b) and 1(c)]. The full description of grain ordering would include an additional order parameter characterizing the local positional alignment of grains. However, for the sake of simplicity we chose to neglect this additional ordering and remain in the framework of nematodynamics. Furthermore, the continuum description implies that the correlation length of the ordered state is much larger than the grain size. We should note that, in our experiments, the correlation length of the local nematic order was rather short (of the order of a grain length in the direction along the grain and 5–6 grain widths in the orthogonal direction), which is why our continuum description can be valid only qualitatively. However, our description is rather generic and can be relevant for other experimental studies such as Ref. [15] where the nematic order is more pronounced.

One of the surprising experimental observations was a very strong sensitivity of swirling to the shape of the particles: for example, no swirling or smectic ordering was observed for monodisperse metal cylindrical particles. Very little swirling was observed for Basmati rice also. While we do not know the exact mechanism of this strong sensitivity, in the framework of our model this effect can be possibly explained by variations of the effective elastic constants $D_{1,2}$, due to interlocking of particles and formation of tetratic structures. Tetratic structures possibly possess higher rigidity and resistance to shear, driving the system below the threshold of swirling instability.

The horizontal acceleration responsible for swirling was an unintended and uncontrolled feature of our shaker system. It showed a strong resonant behavior near a certain vibration frequency. This behavior is common for any mechanical shaker system; however, in other experimental setups this component may be smaller or larger, or it may peak at different oscillation frequencies. That possibly explains why other experimental groups observed swirling motion at different experimental conditions [15]. A shaker system with a controllable and tunable horizontal component of vibration like that in Ref. [26] could provide further insight into the nature of swirling motion.

ACKNOWLEDGMENTS

We thank Alex Snezhko for his help with the experiment, and Hugues Chate, Arshad Kudrolli, and Christof Kruelle for useful discussions. We are also grateful to anonymous referees for their constructive criticism. This work was supported by U.S. DOE Grants No. DE-AC02-06CH11357 (ANL) and No. DE-FG02-04ER46135 (UCSD).

[1] I. S. Aranson and L. S. Tsimring, Rev. Mod. Phys. **78**, 641 (2006).
[2] D. Helbing, Rev. Mod. Phys. **73**, 1067 (2001).
[3] J. Toner, Y. Tu, and S. Ramaswamy, Ann. Phys. **318**, 170 (2005).
[4] T. Vicsek, A. Czirók, E. Ben-Jacob, I. Cohen, and O. Shochet, Phys. Rev. Lett. **75**, 1226 (1995).
[5] G. Grégoire and H. Chaté, Phys. Rev. Lett. **92**, 025702 (2004).
[6] H. Chaté, F. Ginelli, and R. Montagne, Phys. Rev. Lett. **96**, 180602 (2006).
[7] P. Kraikivski, R. Lipowsky, and J. Kierfeld, Phys. Rev. Lett. **96**, 258103 (2006).
[8] X.-L. Wu and A. Libchaber, Phys. Rev. Lett. **84**, 3017 (2000).
[9] C. Dombrowski, L. Cisneros, S. Chatkaew, R. E. Goldstein, and J. O. Kessler, Phys. Rev. Lett. **93**, 098103 (2004).
[10] I. H. Riedel, K. Kruse, and J. Howard, Science **309**, 300 (2005).
[11] A. Sokolov, I. S. Aranson, R. E. Goldstein, and J. O. Kessler, Phys. Rev. Lett. **98**, 158102 (2007).
[12] I. S. Aranson and L. S. Tsimring, Phys. Rev. E **71**, 050901(R) (2005); **74**, 049907 (2006).
[13] D. L. Blair, T. Neicu, and A. Kudrolli, Phys. Rev. E **67**, 031303 (2003).
[14] I. S. Aranson and L. S. Tsimring, Phys. Rev. E **67**, 021305 (2003).
[15] V. Narayan, N. Menon, and S. Ramaswamy, J. Stat. Mech.: Theory Exp. P01005 (2006).
[16] Earlier works on monolayers of vibrated granular rods had mostly focused on the nature of the isotropic-nematic phase transition with the increase of the filling fraction; see F. X. Villarruel, B. E. Lauderdale, D. M. Mueth, and H. M. Jaeger, Phys. Rev. E **61**, 6914 (2000); J. Galanis, D. Harries, D. L. Sackett, W. Losert, and R. Nossal, Phys. Rev. Lett. **96**, 028002 (2006).
[17] D. Volfson, A. Kudrolli, and L. S. Tsimring, Phys. Rev. E **70**, 051312 (2004).
[18] Anisotropy alone is not sufficient for swirling: earlier experiments [15] show that flat-headed (cylindrical) particles form tetratic structures instead of nematic order and swirls. This suggests that the interaction among particles is also crucial for forming nematic states: tapered ends of rice grains make it easy for them to slide past each other.
[19] I. S. Aranson, A. Sokolov, R. E. Goldstein, and J. O. Kessler, Phys. Rev. E **75**, 040901 (2007).
[20] I. S. Aranson, D. Blair, W. K. Kwok, G. Karapetrov, U. Welp, G. W. Crabtree, V. M. Vinokur, and L. S. Tsimring, Phys. Rev. Lett. **82**, 731 (1999).
[21] M. V. Sapozhnikov, I. S. Aranson, and J. S. Olafsen, Phys. Rev. E **67**, 010302(R) (2003).
[22] See EPAPS Document No. E-PLEEE8-75-053704 for experimental movies of swirling motion. See also http://inls.ucsd.edu/grain/rice. For more information on EPAPS, see http://www.aip.org/pubservs/epaps.html.
[23] E. A. Cowen and J. K. Sveen, in *PIV and Water Waves*, edited by J. Grue, P. L. F. Liu, and G. Pedersen (World Scientific, Singapore, 2003), pp. 1–49.
[24] In Ref. [15] it was suggested that the rotation is associated with the misalignment of particles at the boundary of the container.
[25] F. J. C. Rademacher and L. Ter Borg, Eng. Res. **60**, 261 (1994); E. M. Sloot and N. P. Kruyt, Powder Technol. **89**, 203 (1996).
[26] R. Grochowski, P. Walzel, M. Rouijaa, C. A. Kruelle, and I. Rehberg, Appl. Phys. Lett. **84**, 1019 (2004).
[27] Interactive Data Language, ITT Visual Information Solutions, http://www.ittvis.com
[28] F. Rouyer and N. Menon, Phys. Rev. Lett. **85**, 3676 (2000).
[29] K. Kohlstedt, A. Snezhko, M. V. Sapozhnikov, I. S. Aranson, J. S. Olafsen, and E. Ben-Naim, Phys. Rev. Lett. **95**, 068001 (2005).
[30] P.-G. de Gennes and J. Prost, *The Physics of Liquid Crystals* (Clarendon Press, Oxford, 1995).
[31] K. Kruse, J. F. Joanny, F. Jülicher, J. Prost, and K. Sekimoto, Phys. Rev. Lett. **92**, 078101 (2004).
[32] S. Ramaswamy, R. A. Simha, and J. Toner, Europhys. Lett. **62**, 196 (2003).
[33] R. A. Simha and S. Ramaswamy, Phys. Rev. Lett. **89**, 058101 (2002).
[34] Y. Hatwalne, S. Ramaswamy, M. Rao, and R. A. Simha, Phys. Rev. Lett. **92**, 118101 (2004).
[35] Local nematic ordering in our system occurs even for particle aspect ratios (2–4) significantly lower than predicted by molecular dynamics simulations of hard needles at thermal equilibrium (critical aspect ratio is 6); see, e.g., D. Frenkel and R. Eppenga, Phys. Rev. A **31**, 1776 (1985). We believe that this discrepancy is related to the nonequilibrium character of the particle driving and interaction with each other. As one evidence of the very complex nature of nematic ordering in systems of elongated grains, in Ref. [15] the nematic ordering was observed only for long enough particles with tapered ends (like rice or rolling pins), whereas particles with nontapered ends (rods or cylinders) typically formed only defect-riddled locally ordered nematic states.
[36] The conveying force is highly variable on the time scale of vertical vibrations (horizontal impulse is transmitted when one of the ends of a grain touches the plate surface); however, we are interested in the conveying force averaged over the period of vibrations.
[37] S. Dorbolo, D. Volfson, L. Tsimring, and A. Kudrolli, Phys. Rev. Lett. **95**, 044101 (2005).